Journal of Computational Physics 513 (2024) 113196

Contents lists available at ScienceDirect

Journal of Computational Physics

journal homepage: www.elsevier.com/locate/jcp

Mass lumping the dual cell method to arbitrary polynomial degree for acoustic and electromagnetic waves

Markus Wess [a,*], Bernard Kapidani [b], Lorenzo Codecasa [c], Joachim Schöberl [a]

[a] Institute of Analysis and Scientific Computing, Technische Universität Wien, A-1040, Vienna, Austria
[b] Institute of Mathematics, École Polytechnique Féd'erale Lausanne, CH-1015 Lausanne, Switzerland
[c] Dipartimento di Elettronica, Informatica e Bioingegneria, Politecnico di Milano, I-20133 Milano, Italy

ARTICLE INFO

Keywords:
Time-domain Maxwell equations
Cell method
Discontinuous Galerkin
Dual grids
Mass lumping
High-order finite elements

ABSTRACT

We present a fundamental improvement of a high polynomial degree time domain cell method recently introduced by the last three authors. The published work introduced a method featuring block-diagonal system matrices where the block size and conditioning scaled poorly with respect to polynomial degree. The issue is herein bypassed by the construction of new basis functions exploiting quadrature rule based mass lumping techniques for arbitrary polynomial degrees in two dimensions for the Maxwell equations and the acoustic wave equation in the first order velocity pressure formulation. We characterize the degrees of freedom of all new discrete approximation spaces we employ for differential forms and show that the resulting block diagonal (inverse) mass matrices have block sizes independent of the polynomial degree. We demonstrate on an extensive number of examples how the new technique is applicable and efficient for large scale computations.

1. Introduction

When solving time dependent initial boundary value problems for hyperbolic partial differential equations such as the Maxwell system or the acoustic wave equation, the most used choice for the space discretization is finite differences (usually the second order accurate version, on staggered grids). This is due to their massively parallelisable nature and the fact that they are easy to implement. Especially the first point is of great importance for the simulation of large scale problems, e.g., in the context of seismic imaging or the simulation of electromagnetic waves in photonic crystals [1,2]. Nevertheless, since the work of Hesthaven & Warburton [3] on discontinuous Galerkin (DG) Finite Element Methods (FEM) there has been a revitalized enthusiasm in using variational methods to discretize the Maxwell system in a way that leads to block diagonal mass matrices even on unstructured grids.

The present manuscript fits in this framework and, while building originally on low order Finite Integration Techniques (FIT, [4,5]), is a instead high-order accurate like the DG approach and acts as a follow up on a recent paper [6] by three of the present authors. There a new high order discontinuous Galerkin (DG) method on primal-dual unstructured grids was introduced for the 2D Maxwell equations. The method can be used to efficiently discretize (electromagnetic and acoustic) wave equations in first order form. One of the two unknown fields is discretized in a piecewise conforming way on the original, also called primal, triangulation

* Corresponding author.
E-mail addresses: markus.wess@tuwien.ac.at (M. Wess), bernard.kapidani@epfl.ch (B. Kapidani), lorenzo.codecasa@polimi.it (L. Codecasa), joachim.schoeberl@tuwien.ac.at (J. Schöberl).

https://doi.org/10.1016/j.jcp.2024.113196
Received 22 December 2023; Received in revised form 5 June 2024; Accepted 9 June 2024

Available online 13 June 2024

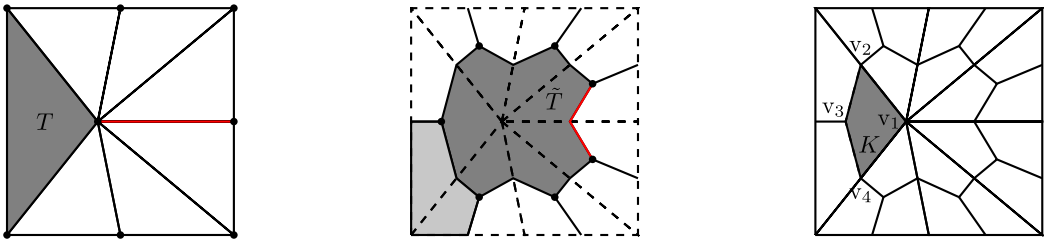

Fig. 1. From left to right, we first mesh the unit square $\Omega = (0,1) \times (0,1)$ leading to the triangulation $\mathcal{T}_h$ (we show one triangle $T \in \mathcal{T}_h$). We then construct the barycentric-dual complex: $\tilde{T} \in \tilde{\mathcal{T}}_h$ is dual to a vertex in $\mathcal{T}_h$. We show in light gray the case of a dual cell corresponding a to a vertex on the boundary of Ω and in darker gray a dual cell for an internal vertex. We finally highlight the resulting quadrilateral mesh $\mathcal{K}_h$ where we emphasize a micro-cell K. (For interpretation of the colors in the figure(s), the reader is referred to the web version of this article.)

while the other, which we will refer to as the dual unknown, is piecewise conforming on a barycentric dual, generally polygonal, mesh. This approach, although unconventional, has several enticing features:

1. There is no need to penalize jumps in the solutions or numerically (i.e., artificially) dissipate energy to achieve spectral correctness of the method (as for some DG approaches, e.g., [3]).
2. Similarly to DG methods, it leads to block diagonal mass matrices which provide the amenability to parallelization for HPC implementations.

On the other hand, open problems remain. The main drawbacks of the previously published work were the following:

1. The blocks in the discrete mass matrix for the dual unknown grow in size with polynomial degree considerably due to the potentially many elements in the original mesh sharing a vertex and the conformity conditions across edges. This is, for example, not the case for the original DG approach which has small fixed size blocks in the mass matrix when increasing the polynomial degree, due to the use of orthogonal polynomials as basis functions.
2. the local monomial basis used for approximating both primal and dual unknowns is dramatically ill-conditioned for increasing polynomial degree P, spoiling P–refinement approaches, which is exactly the setting in which DG methods are supposed to shine.

Fortunately, neither of the aforementioned drawbacks is inherent to the method. Both depend on the choice made for local approximation spaces and their basis functions. By focusing on the quadrilateral mesh generated by the intersection of primal and dual meshes, we can recast the method as a DG-FEM method using quadrilaterals as the basic domain of definition of its approximation spaces. With respect to [6], we switch from the space $\mathcal{P}^P(K)$ of bivariate polynomials of total degree at most P to the space $\mathcal{Q}^P(\hat{K})$ of polynomials of degree at most P separately in each variable on the reference square $\hat{K}$. Subsequently we compose the polynomial basis functions on $\hat{K}$ with appropriate push-forwards to generic quadrilaterals K to obtain a basis on the physical primal and dual elements.

After a brief recap of the main ingredients in Section 2, we show how the new formulations address both issues in Section 3. Numerical examples validate the improved convergence and efficiency of the new approach in Section 4 and conclusions are thereby drawn in the final section.

2. Mass lumping on barycentric dual meshes

In the present section we provide the notation and basic ingredients for our formulations. We first introduce dual meshes in Section 2.1. Once the quadrilateral nature of the global mesh given by the dual cell method is established, we define polynomial approximation spaces on a reference square in Section 2.3. Finally, we provide the recipe to push-forward and glue the local basis functions into global DG spaces similar to the ones presented in [6].

2.1. Barycentric-dual meshes

We assume a triangulation $\mathcal{T}_h$ of the spatial domain $\Omega \subset \mathbf{R}^2$ (in the sense of [7]) to be available such that $\cup_{T \in \mathcal{T}_h} \overline{T} = \overline{\Omega}$, where the overline denotes the closure of a set. We make the usual assumptions on conforming meshing of discontinuities in the material parameters and call this starting mesh the *primal* mesh when necessity arises. We construct in fact a dual mesh for $\mathcal{T}_h$ which we denote by $\tilde{\mathcal{T}}_h$. We perform the construction as in all previous related work on the cell method by taking centroids of triangles as dual vertices and connecting them through segments to the midpoints (centroids) of (primal mesh) edges. If a primal edge is part of $\partial\Omega$ there is only one such segment originating from the midpoint of the edge. If this is not the case, the union of any two such segments meeting in the centroid of an edge is a poly-line. We call both cases a dual edge, noting that this procedure builds a natural isomorphism between primal and dual edges. To complete the construction we obtain a family of two-dimensional sets, called dual cells since they are not necessarily triangles. In fact for each vertex in the interior of Ω the corresponding dual cell $\tilde{T} \in \tilde{\mathcal{T}}_h$ is a

(generally non-convex) polygon bounded by dual edges (e.g., the darker gray cell in the second panel of Fig. 1). For each vertex in $\partial\Omega$ there are instead exactly two edges originating from this vertex. The segments connecting the vertex to their midpoints then complete the boundary of the dual cell (e.g., the lighter gray cell in the second panel of Fig. 1). The barycentric dual procedure outlined above results in a third derived quadrilateral mesh, which is what we are ultimately going to discretize the target partial differential equations with and which we denote by $\mathcal{K}_h$. We will also call the quadrilaterals in these mesh micro-cells, to distinguish them from the primal and dual cells.

We introduce local coordinates for the vertices $\mathbf{v}_K^1, \mathbf{v}_K^2, \mathbf{v}_K^3, \mathbf{v}_K^4 \in \mathbb{R}^2$ for each quadrilateral subdomain $K \in \mathcal{K}_h$ (located e.g., as in the rightmost panel of Fig. 1) resulting from a non empty intersection of a primal and dual cell. Without loss of generality we always choose $\mathbf{v}_K^1$ to coincide with a vertex of the primal mesh and the remaining vertices arranged following a counter-clockwise loop around the quadrilateral. This implies that $\mathbf{v}_K^3$ (which in conjunction with $\mathbf{v}_K^1$ uniquely identifies the quadrilateral K) is always the centroid of a triangle in the primal mesh. A physical quadrilateral is then uniquely determined by the continuous and invertible bilinear mapping $\mathbf{F}_K : \hat{K} := [0,1]^2 \to \overline{K}$, that sends vertices of the unit square into vertices of K, i.e., the unique vector valued mapping $\mathbf{F}_K$

$$\mathbf{F}_K(\xi,\eta) := (1-\xi)(1-\eta)\mathbf{v}_K^1 + \xi(1-\eta)\mathbf{v}_K^2 + \xi\eta\mathbf{v}_K^3 + (1-\xi)\eta\mathbf{v}_K^4, \tag{1}$$

which we remark being a standard mapping choice for quadrilateral finite element families (the other being the choice of $[-1,1]\times[-1,1]$ as a reference square domain). We denote by $\mathbf{dF}_K$ the Jacobian matrix associated to $\mathbf{F}_K$, i.e. the 2×2 matrix:

$$\mathbf{dF}_K = \begin{pmatrix} (\mathbf{v}_K^2 - \mathbf{v}_K^1)(1-\eta) + (\mathbf{v}_K^3 - \mathbf{v}_K^4)\eta & (\mathbf{v}_K^4 - \mathbf{v}_K^1)(1-\xi) + (\mathbf{v}_K^2 - \mathbf{v}_K^3)\xi \end{pmatrix},$$

and $J_K = J_K(\xi,\eta)$ its determinant, which is a bilinear polynomial in ξ and η.
Since the parametrization $\mathbf{F}_K$ and its inverse are smooth on each quadrilateral, we may define several pushforwards (and pullbacks) for scalar and vector valued functions under change of coordinates from (and to) the unit square to (and from) the physical quadrilateral. The following standard definitions, well known from the FEM literature on de Rham sequences of Finite Element spaces (such as [8]) apply locally:

$$\begin{aligned} u(x,y) &:= \imath_K^{\mathrm{grad}}(\hat{u}) := \hat{u}\circ\mathbf{F}_K^{-1}, && \hat{u} \in \hat{Q}_P, \\ \boldsymbol{v}(x,y) &:= \imath_K^{\mathrm{curl}}(\hat{\boldsymbol{v}}) := (\mathbf{dF}_K)^{-\top}(\hat{\boldsymbol{v}}\circ\mathbf{F}_K^{-1}), && \hat{\boldsymbol{v}} \in [\hat{Q}_P]^2, \\ \boldsymbol{w}(x,y) &:= \imath_K^{\mathrm{div}}(\hat{\boldsymbol{w}}) := J_K^{-1}(\mathbf{dF}_K)(\hat{\boldsymbol{w}}\circ\mathbf{F}_K^{-1}), && \hat{\boldsymbol{w}} \in [\hat{Q}_P]^2, \end{aligned} \tag{2}$$

where the overhead hat denotes fields defined on the reference square and we denote the space of scalar valued polynomials of degree P with $\hat{Q}_P$ and $\boldsymbol{v}$, $\boldsymbol{w}$ and u are vector (in boldface) and scalar valued square-integrable functions on K. The superscripts grad, curl, and div, are due to the fact that the three pushforwards are designed to respectively preserve point values, tangential traces and normal traces of their argument function under changes of coordinates. Since the mappings in Eq. (2) are invertible, we can then easily deduce the expression of the pullbacks through algebraic inversion.

2.2. Mass-lumped inner products

In the following we define the approximate (mass lumped) inner products we use in our numerical method. We start by considering the closed interval $\hat{I} = [0,1]$ and the Legendre–Gauss–Radau (LGR) quadrature nodes with fixed endpoint in the local variable $\xi \in \hat{I}$, which consist of $P+1$ points $\{\xi_i\}_{i=0}^P$. They are standard in the literature (e.g. in [9, Chapter 10.6]) and we assume the points to be sorted in ascending order with $\xi_P = 1$. These nodes, with appropriate weights $\{w_i\}_{i=0}^P$, are computed such that integrals of polynomials of degree $2P$ are exactly computable on the unit interval, i.e., if $f(\xi)$ is a polynomial of degree at most $2P$ there holds

$$\int_0^1 f(\xi)\,\mathrm{d}\xi = \sum_{i=0}^P w_i f(\xi_i). \tag{3}$$

We define a second set of LGR nodes on the interval $[0,1]$, namely the set $\{\tilde{\xi}_i\}_{i=0}^P$ by $\tilde{\xi}_{P-i} = 1-\xi_i$. Through obvious symmetry arguments the second, dual set has the same approximation properties as the primal one for numerical integration, when provided with the corresponding dual weights $\{\tilde{w}_i\}_{i=0}^P$ (in fact $\tilde{w}_i = w_{P-i}$).

We can use $\{\xi_i\}_{i=0}^P$ to define an interpolatory polynomial basis in a straightforward way: the i-th Lagrangian polynomial of degree P based on the primal LGR quadrature nodes, denoted as $\hat{\ell}_P^{(i)}(\xi)$, is defined as the unique polynomial of degree P such that

$$\hat{\ell}_P^{(i)}(\xi_j) = \delta_{ij},$$

where δ_{ij} is the Kronecker delta. We can likewise define $\tilde{\hat{\ell}}_P^{(i)} \in \mathcal{P}^P(\hat{I})$ with the analogous Kronecker delta property: $\tilde{\hat{\ell}}_P^{(i)}(\tilde{\xi}_j) = \delta_{ij}$. Next, we consider the tensorization of these Lagrangian polynomials to extend them from one to two variables (i.e., from $\hat{I}$ to $\hat{K}$). To construct the tensorized Lagrangian polynomials, we define the tensor product of two one-dimensional Lagrangian polynomials $\hat{\ell}_P^{(i)}(\xi)$ and $\hat{\ell}_P^{(j)}(\eta)$

$$\hat{\ell}_P^{(i,j)}(\xi,\eta) = \hat{\ell}_P^{(i)}(\xi)\hat{\ell}_P^{(j)}(\eta),$$
$$\tilde{\hat{\ell}}_P^{(i,j)}(\xi,\eta) = \tilde{\hat{\ell}}_P^{(i)}(\xi)\tilde{\hat{\ell}}_P^{(j)}(\eta).$$

These bivariate polynomials generate the space

$$\hat{Q}_P = \mathrm{span}\{\hat{\ell}_P^{(i,j)}(\xi,\eta)\} = \mathrm{span}\{\tilde{\hat{\ell}}_P^{(i,j)}(\xi,\eta)\},$$

which is the space of polynomials of degree up to P in each variable ξ, η. Similarly one can define vector valued functions:

$$\hat{\boldsymbol{\ell}}_P^{(i,j,k)}(\xi,\eta) = \hat{\ell}_P^{(i)}(\xi)\hat{\ell}_P^{(j)}(\eta)\hat{\mathbf{e}}_k,$$
$$\tilde{\hat{\boldsymbol{\ell}}}_P^{(i,j,k)}(\xi,\eta) = \tilde{\hat{\ell}}_P^{(i)}(\xi)\tilde{\hat{\ell}}_P^{(j)}(\eta)\hat{\mathbf{e}}_k,$$

where $\hat{\mathbf{e}}_k$ with $k \in \{1,2\}$ are the unit Euclidean vectors, i.e., $\hat{\mathbf{e}}_1 = (1\ 0)^\top$, $\hat{\mathbf{e}}_2 = (0\ 1)^\top$, and it follows:

$$[\hat{Q}_P]^2 = \mathrm{span}\{\hat{\boldsymbol{\ell}}_P^{(i,j,1)}\} \oplus \mathrm{span}\{\hat{\boldsymbol{\ell}}_P^{(i,j,2)}\} = \mathrm{span}\{\tilde{\hat{\boldsymbol{\ell}}}_P^{(i,j,1)}\} \oplus \mathrm{span}\{\tilde{\hat{\boldsymbol{\ell}}}_P^{(i,j,2)}\}, \tag{4}$$

where $\oplus$ denotes the direct sum of vector spaces. We remark that, extending the integration rule of (3) to two dimensions we can define the approximate inner product, for both scalar functions $\hat{f}, \hat{g} \in C(\hat{K})$ and vector valued functions $\hat{\boldsymbol{u}}, \hat{\boldsymbol{v}} \in [C(\hat{K})]^2$, given by

$$\left\langle \hat{f}, \hat{g} \right\rangle_{\hat{K}}^P := \sum_{i=0}^{P}\sum_{j=0}^{P} w_i w_j \hat{f}(\xi_i,\xi_j)\hat{g}(\xi_i,\xi_j) \approx \int_0^1 \mathrm{d}\eta \int_0^1 \mathrm{d}\xi\, \hat{f}(\xi,\eta)\hat{g}(\xi,\eta), \tag{5}$$

$$\langle \hat{\boldsymbol{u}}, \hat{\boldsymbol{v}} \rangle_{\hat{K}}^P := \sum_{i=0}^{P}\sum_{j=0}^{P} w_i w_j \hat{\boldsymbol{u}}(\xi_i,\xi_j)\cdot\hat{\boldsymbol{v}}(\xi_i,\xi_j) \approx \int_0^1 \mathrm{d}\eta \int_0^1 \mathrm{d}\xi\, \hat{\boldsymbol{u}}(\xi,\eta)\cdot\hat{\boldsymbol{v}}(\xi,\eta), \tag{6}$$

where the same notation will be used for inner products computed using dual integration rules. This is a slight abuse of notation, but the choice of the integration rule based on $\{\tilde{\xi}_i\}_{i=0}^P$ rather than $\{\xi_i\}_{i=0}^P$ will be obvious from the context in Section 3. We call these inner products *mass-lumped* inner products. Likewise the following properties which we present for the primal integration nodes can be stated nearly verbatim for the dual ones. Therefore in the following paragraphs we only go into detail for the primal integration rules.

On the reference square it is easy to see that the following exact orthogonality properties hold:

$$\left\langle \hat{\ell}_P^{(i,j)}, \hat{\ell}_P^{(l,m)} \right\rangle_{\hat{K}}^P = w_i w_j \delta_{il}\delta_{jm},$$
$$\left\langle \hat{\boldsymbol{\ell}}_P^{(i,j,k)}, \hat{\boldsymbol{\ell}}_P^{(l,m,n)} \right\rangle_{\hat{K}}^P = w_i w_j \delta_{il}\delta_{jm}\delta_{kn},$$

where δ is again the Kronecker symbol. We remark that the inner products above are actually identical to the L^2 inner products, since the integrands are polynomials of degree $2P$. Both properties will be pivotal in the following.

We can thus define how our approximate inner products then look like on the physical quadrilateral K in the mesh for scalar continuous functions f, g on K, based on LGR integration rules

$$\langle f, g \rangle_K^P := \langle J_K f \circ \mathbf{F}_K, g \circ \mathbf{F}_K \rangle_{\hat{K}}^P, \tag{7}$$

with the obvious same definition for vector-valued $\langle \boldsymbol{u}, \boldsymbol{v} \rangle_{\hat{K}}^P$ and continuous $\boldsymbol{u}, \boldsymbol{v}$.

In the particular case in which $u, \boldsymbol{v}, \boldsymbol{w}$ (and $u', \boldsymbol{v}', \boldsymbol{w}'$) are push-forwards as in Eq. (2) we obtain

$$\left\langle u, u' \right\rangle_K^P = \left\langle \imath_K^{\mathrm{grad}}(\hat{u})\circ\mathbf{F}_K, \imath_K^{\mathrm{grad}}(\hat{u}')\circ\mathbf{F}_K \right\rangle_{\hat{K}}^P = \left\langle \hat{u}, J_K \hat{u}' \right\rangle_{\hat{K}}^P,$$
$$\left\langle \boldsymbol{v}, \boldsymbol{v}' \right\rangle_K^P = \left\langle \imath_K^{\mathrm{curl}}(\hat{\boldsymbol{v}})\circ\mathbf{F}_K, \imath_K^{\mathrm{curl}}(\hat{\boldsymbol{v}}')\circ\mathbf{F}_K \right\rangle_{\hat{K}}^P = \left\langle \hat{\boldsymbol{v}}, \mathbb{G}^K \hat{\boldsymbol{v}}' \right\rangle_{\hat{K}}^P,$$
$$\left\langle \boldsymbol{w}, \boldsymbol{w}' \right\rangle_K^P = \left\langle \imath_K^{\mathrm{div}}(\hat{\boldsymbol{w}})\circ\mathbf{F}_K, \imath_K^{\mathrm{div}}(\hat{\boldsymbol{w}}')\circ\mathbf{F}_K \right\rangle_{\hat{K}}^P = \left\langle \hat{\boldsymbol{w}}, \mathbb{H}^K \hat{\boldsymbol{w}}' \right\rangle_{\hat{K}}^P,$$

where we have absorbed the (smooth) Jacobian determinant of the mapping within one inner product argument without loss of generality. We furthermore used the symmetric matrices:

$$\mathbb{G}^K = (\mathbf{dF}_K)^{-1} J_K (\mathbf{dF}_K)^{-\top},$$
$$\mathbb{H}^K = (\mathbf{dF}_K)^{\top} J_K^{-1} (\mathbf{dF}_K),$$

where we have omitted for readability the dependence of all quantites on ξ and η and it is clear that $\mathbb{G}^K \mathbb{H}^K = \mathbb{I}^{2\times 2}$. The following (quasi) orthogonality conditions then hold:

$$\left\langle \imath_K^{\mathrm{grad}}(\hat{\ell}_P^{(i,j)}), \imath_K^{\mathrm{grad}}(\hat{\ell}_P^{(l,m)}) \right\rangle_K^P = w_i w_j \delta_{il}\delta_{jm} J_K(\xi_i,\xi_j),$$

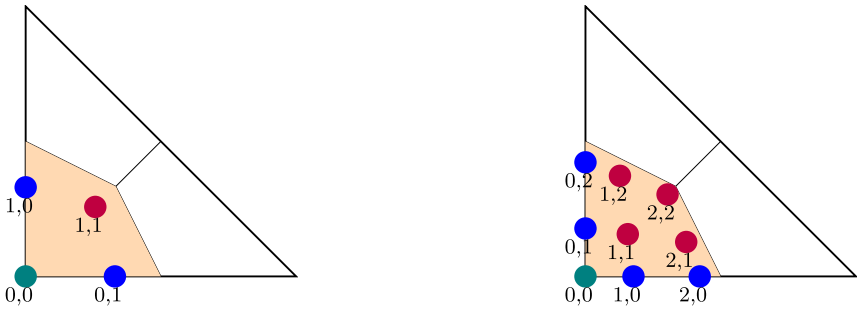

(a) $P = 1$ (b) $P = 2$

Fig. 2. Points associated to the degrees of freedom (DoFs) of $X_1^{\mathrm{grad}}(\tilde{\mathcal{T}}_h)$ and $X_2^{\mathrm{grad}}(\tilde{\mathcal{T}}_h)$ on one quadrilateral. Red dots correspond to basis functions u_i^K, blue ones to u_i^E and teal ones to u^V.

$$\left\langle \imath_K^{\mathrm{curl}}(\hat{\boldsymbol{\ell}}_P^{(i,j,k)}), \imath_K^{\mathrm{curl}}(\hat{\boldsymbol{\ell}}_P^{(l,m,n)}) \right\rangle_K^P = w_i w_j \delta_{il}\delta_{jm}(\mathbb{G}^K)_{kn}(\xi_i,\xi_j),$$
$$\left\langle \imath_K^{\mathrm{div}}(\hat{\boldsymbol{\ell}}_P^{(i,j,k)}), \imath_K^{\mathrm{div}}(\hat{\boldsymbol{\ell}}_P^{(l,m,n)}) \right\rangle_K^P = w_i w_j \delta_{il}\delta_{jm}(\mathbb{H}^K)_{kn}(\xi_i,\xi_j),$$

where $(\mathbb{G}^K)_{kn}(\xi_i,\xi_j)$ is the (k,n)-th entry of the matrix $\mathbb{G}^K$ evaluated at coordinates (ξ_i,ξ_j) and $(\mathbb{H}^K)_{kn}(\xi_i,\xi_j)$ is the (k,n)-th entry of the matrix $\mathbb{H}^K$ evaluated at coordinates (ξ_i,ξ_j). Since $k,n \in \{1,2\}$, assembling the last two above expressions into inner-product matrices yields 2-by-2 block diagonal matrices.

2.3. Nodal spaces on dual cells

Now that we have defined the mass-lumped inner products we focus on the construction of the (local) bases of our approximation spaces. Again the construction is very similar for the primal and dual bases. Since it is the more exotic case, we focus on the construction of the dual spaces.

We choose the degrees of freedom of our spaces to be point values of the respective fields in the integration points defined above to exploit the orthogonalites derived in the previous subsection. To this end we take a dual cell $\tilde{T} \in \tilde{\mathcal{T}}_h$. This is the union of a finite number of quadrilaterals K on which we construct three types of discrete spaces $\tilde{X}_P^{\mathrm{grad}}(\tilde{T})$, $\tilde{X}_P^{\mathrm{curl}}(\tilde{T})$, $\tilde{X}_P^{\mathrm{div}}(\tilde{T})$ spanned by piecewise polynomials.

2.3.1. Basis functions for $\tilde{X}_P^{\mathrm{grad}}(\tilde{T})$

We start by remarking that for a given dual cell $\tilde{T}$ there exists exactly one vertex V of the primal such that $V \in \overline{\tilde{T}}$. Then the function which is interpolatory at V, defined by

$$u^V(\boldsymbol{x}) = \begin{cases} \imath_K^{\mathrm{grad}}(\hat{\ell}_P^{(0,0)}) & \text{if } \boldsymbol{x} \in K \subset \tilde{T} \quad \forall K \text{ s.t. } V \in \partial K, \\ 0 & \text{otherwise,} \end{cases}$$

is continuous on $\tilde{T}$ (cf., Fig. 2, DoFs with index $(0,0)$ and Fig. 3a). Additionally, we have edge functions: for each edge E originating from V in the skeleton of $\mathcal{K}_h$, there are two quadrilaterals K_L, K_R for which $E \subseteq \partial K_L$ and $E \subseteq \partial K_R$ (cf., Fig. 3b), where the subscripts stand for left and right respectively and are motivated by the right-handed corkscrew rule providing an inner orientation for $\tilde{T}$. There are then P basis functions of the kind:

$$u_i^E(\boldsymbol{x}) = \begin{cases} \imath_{K_L}^{\mathrm{grad}}(\hat{\ell}_P^{(0,i)}) & \text{if } \boldsymbol{x} \in K_L, \\ \imath_{K_R}^{\mathrm{grad}}(\hat{\ell}_P^{(i,0)}) & \text{if } \boldsymbol{x} \in K_R, \\ 0 & \text{otherwise,} \end{cases}$$

with $i = 1,\dots,P$. We remark that the definition trivially extends to the case in which $E \subset \partial\Omega$ where we simply have either $K_L = \emptyset$ or $K_R = \emptyset$.

Finally, for each quadrilateral $K \subset \tilde{T}$ there are P^2 functions of the kind:

$$u_{(j-1)P+i}^K(\boldsymbol{x}) = \begin{cases} \imath_K^{\mathrm{grad}}(\hat{\ell}_P^{(i,j)}) & \text{if } \boldsymbol{x} \in K \subset \tilde{T}, \\ 0 & \text{otherwise,} \end{cases}$$

with $i,j = 1,\dots,P$. We remark that these basis functions are compactly supported on a single quadrilateral K (cf., Fig. 3c).

We then define $\tilde{X}_P^{\mathrm{grad}}(\tilde{T})$ as the span of the union of the three sets of basis functions above and remark that $\tilde{X}_P^{\mathrm{grad}}(\tilde{T}) \subset \mathrm{H}^1(\tilde{T})$ where $\mathrm{H}^1(\tilde{T})$ is the space of square integrable functions on $\tilde{T}$ with square integrable gradient, i.e.,

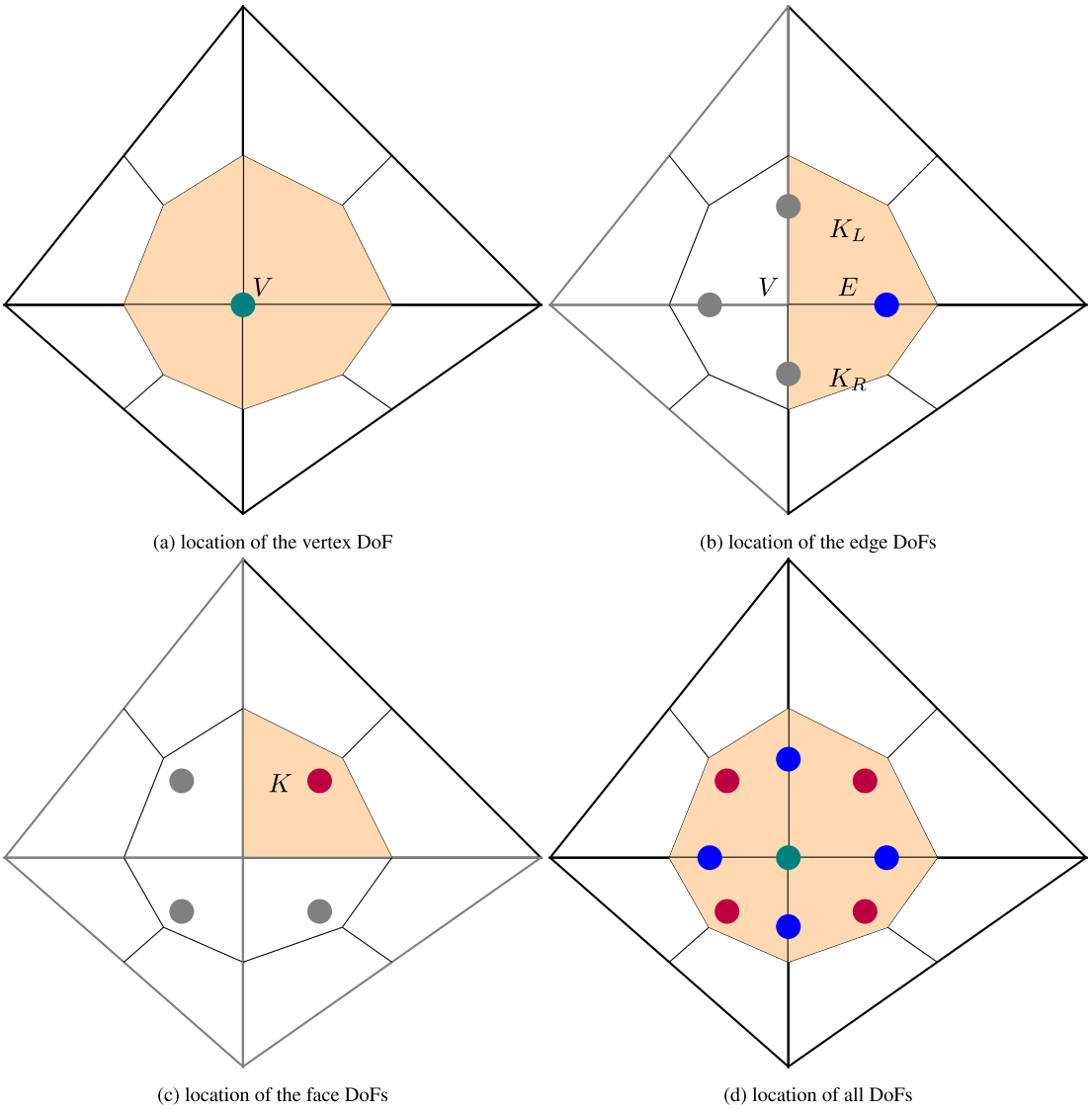

(a) location of the vertex DoF (b) location of the edge DoFs

(c) location of the face DoFs (d) location of all DoFs

Fig. 3. Points associated to the vertex, edge and face DoFs Figs. 3a to 3c of $X_1^{\mathrm{grad}}(\tilde{\mathcal{T}}_h)$ on one element of the dual mesh (Fig. 3d colored). The colored quadrilaterals mark the support of the basis function corresponding to the colored DoF, where the same color coding as in Fig. 2 applies.

$$\mathrm{H}^1(\tilde{T}) = \left\{ u \in \mathrm{L}^2(\tilde{T}) : \operatorname{grad} u \in \mathrm{L}^2(\tilde{T}) \right\}.$$

A pictorial representation of the degrees of freedom on a single quadrilateral for $P = 1$ and $P = 2$ is given in Fig. 2 and for $P = 1$ on a single dual element in Fig. 3.

2.3.2. *Basis functions for* $\tilde{X}_P^{\mathrm{curl}}(\tilde{T})$

For the vector valued space $\tilde{X}_P^{\mathrm{curl}}(\tilde{T})$ we have the following classification of basis functions:

- For each edge $E \subseteq \tilde{T} \setminus \partial\tilde{T}$, again there are two quadrilaterals K_L, K_R for which $E \subseteq \partial K_L$ and $E \subseteq \partial K_R$, as above. There are then $P+1$ basis functions of the kind:

$$\boldsymbol{u}_{i+1}^E(\boldsymbol{x}) = \begin{cases} \iota_{K_L}^{\mathrm{curl}}(\hat{\boldsymbol{r}}_P^{(0,i,2)}) & \text{if } \boldsymbol{x} \in K_L, \\ \iota_{K_R}^{\mathrm{curl}}(\hat{\boldsymbol{r}}_P^{(i,0,1)}) & \text{if } \boldsymbol{x} \in K_R, \\ 0 & \text{otherwise,} \end{cases}$$

with $i = 0, \dots, P$ (note we start from 0). Again the definition trivially extends to the case in which $E \subset \partial\Omega$ where we have simply either $K_L = \emptyset$ or $K_R = \emptyset$.

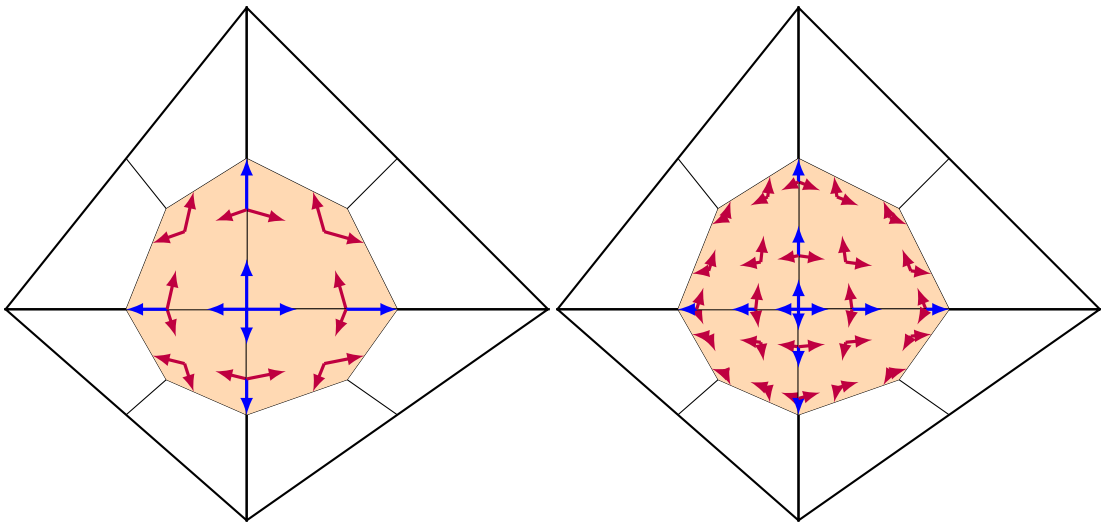

(a) $P = 1$ (b) $P = 2$

Fig. 4. Distribution of the DoFs of $\tilde{X}_1^{\mathrm{curl}}(\tilde{\mathcal{T}}_h)$ and $\tilde{X}_2^{\mathrm{curl}}(\tilde{\mathcal{T}}_h)$ on one dual element (colored).

- For each quadrilateral $K \subset \tilde{T}$ there are $P(P+1)$ functions of the kind:

$$\boldsymbol{u}^K_{(j-1)(P+1)+i+1}(\boldsymbol{x}) = \begin{cases} i_K^{\mathrm{curl}}(\hat{\boldsymbol{\mathscr{C}}}_P^{(i,j,1)}) & \text{if } \boldsymbol{x} \in K \subset \tilde{T}, \\ 0 & \text{otherwise,} \end{cases}$$

with $i = 0, \dots, P$ and $j = 1, \dots, P$ and additional $P(P+1)$ functions of the kind:

$$\boldsymbol{u}^K_{(j-1+P)(P+1)+i+1}(\boldsymbol{x}) = \begin{cases} i_K^{\mathrm{curl}}(\hat{\boldsymbol{\mathscr{C}}}_P^{(i,j,2)}) & \text{if } \boldsymbol{x} \in K \subset \tilde{T}, \\ 0 & \text{otherwise,} \end{cases}$$

with $i = 1, \dots, P$ and $j = 0, \dots, P$. Both kinds of functions above are compactly supported on a single quadrilateral K.

We then define $\tilde{X}_P^{\mathrm{curl}}(\tilde{T})$ as the span of the union of the three sets of basis functions above. A pictorial representation of the degrees of freedom for $P = 1$ and $P = 2$ is given in Fig. 4. We again remark that $\tilde{X}_P^{\mathrm{curl}}(\tilde{T})$ is a subspace of the space $H(\mathrm{curl}; \tilde{T})$ defined as follows:

$$\mathrm{H}(\mathrm{curl}; \tilde{T}) = \left\{ \boldsymbol{v} \in \mathrm{L}^2(\tilde{T})^2 : \mathrm{curl}\, \boldsymbol{v} \in \mathrm{L}^2(\tilde{T})^2 \right\}.$$

The basis functions for $\tilde{X}_P^{\mathrm{div}}(\tilde{T})$ are constructed analogously to the ones for $\tilde{X}_P^{\mathrm{curl}}(\tilde{T})$ and we omit the details here. It suffices to swap Cartesian components in edge based functions and swap i, j iterating indices in basis functions which are instead locally supported on one quadrilateral K. We remark that $\tilde{X}_P^{\mathrm{div}}(\tilde{T})$ is a subspace of the space $H(\mathrm{div}; \tilde{T})$ defined as follows:

$$H(\mathrm{div}; \tilde{T}) = \left\{ \boldsymbol{u} \in \mathrm{L}^2(\tilde{T})^2 : \mathrm{div}\, \boldsymbol{u} \in \mathrm{L}^2(\tilde{T}) \right\}.$$

2.3.3. Construction of the global spaces

Finally, to obtain the discrete spaces on the whole mesh, we define the global space $\tilde{X}_P^{\mathrm{grad}}(\tilde{\mathcal{T}}_h)$ by combining the local spaces $\tilde{X}_P^{\mathrm{grad}}(\tilde{T})$ for all $\tilde{T} \in \tilde{\mathcal{T}}_h$, and similarly for the vector valued fields:

$$\begin{aligned} \tilde{X}_P^{\mathrm{grad}}(\tilde{\mathcal{T}}_h) := &\quad \{u \in \mathrm{L}^2(\tilde{\mathcal{T}}_h) : u|_{\tilde{T}} \in \tilde{X}_P^{\mathrm{grad}}(\tilde{T}), \quad \forall \tilde{T} \in \tilde{\mathcal{T}}_h\}, \\ \tilde{X}_P^{\mathrm{curl}}(\tilde{\mathcal{T}}_h) := &\quad \{\boldsymbol{u} \in [\mathrm{L}^2(\tilde{\mathcal{T}}_h)]^2 : \boldsymbol{u}|_{\tilde{T}} \in \tilde{X}_P^{\mathrm{curl}}(\tilde{T}), \quad \forall \tilde{T} \in \tilde{\mathcal{T}}_h\}, \\ \tilde{X}_P^{\mathrm{div}}(\tilde{\mathcal{T}}_h) := &\quad \{\boldsymbol{u} \in [\mathrm{L}^2(\tilde{\mathcal{T}}_h)]^2 : \boldsymbol{u}|_{\tilde{T}} \in \tilde{X}_P^{\mathrm{div}}(\tilde{T}), \quad \forall \tilde{T} \in \tilde{\mathcal{T}}_h\}, \end{aligned} \tag{8}$$

where degrees of freedom of the global spaces are obtained by the union of the degrees of freedom of the local spaces. We omit the explicit construction of bases for the spaces $X_P^{\mathrm{grad}}(T)$, $X_P^{\mathrm{curl}}(T)$, $X_P^{\mathrm{div}}(T)$ in the case of the primal triangles $T \in \mathcal{T}_h$ since their construction is analogous to what is done above for the case of the dual mesh. We still provide the pictorial representation of the degrees of freedom of the scalar valued space in Fig. 5 and the vector valued one in Fig. 6 for a single triangle in the mesh.

(a) $P = 1$ (b) $P = 2$

Fig. 5. Points associated to the DoFs of $X_P^{\mathrm{grad}}(\mathcal{T}_h)$ for $P = 1, 2$ on one primal element.

(a) $P = 1$ (b) $P = 2$

Fig. 6. Points associated to the DoFs of $X_P^{\mathrm{curl}}(\mathcal{T}_h)$ for $P = 1, 2$ on one primal element.

3. Discrete formulations for waves in 2D

We will now use the notation and tools from the Section 2 to show how to efficiently solve the acoustic and electromagnetic wave equations via the dual cell method in 2D. We will devote specific attention to the similarities and the differences between the mass lumped approach here and the already published approach in [6].

3.1. Maxwell equations

Consider the time-dependent Maxwell equations in their first-order form, solving for an electric field $\boldsymbol{E}(t, \boldsymbol{x}) \in \mathrm{C}^1([0, T]; \mathrm{H}(\mathrm{curl}; \Omega))$ and a magnetic field $H(t, \boldsymbol{x}) \in \mathrm{C}^1([0, T]; \mathrm{H}(\mathrm{rot}; \Omega))$, where we use the symbol rot for the rotated gradient, such that:

$$\varepsilon \frac{\partial \boldsymbol{E}}{\partial t} = \mathrm{rot}\, H - \boldsymbol{J}, \qquad \text{in } \Omega \times (0, T), \tag{9}$$

$$\mu \frac{\partial H}{\partial t} = -\mathrm{curl}\, \boldsymbol{E}, \qquad \text{in } \Omega \times (0, T), \tag{10}$$

$$H = 0, \qquad \text{on } \partial\Omega \times (0, T), \tag{11}$$

$$\boldsymbol{E}(0, \boldsymbol{x}) = \boldsymbol{E}_0(\boldsymbol{x}) \in \mathrm{H}(\mathrm{curl}; \Omega), \quad H(0, \boldsymbol{x}) = H_0(\boldsymbol{x}) \in \mathrm{H}(\mathrm{rot}; \Omega), \qquad \text{in } \Omega, \tag{12}$$

where $\boldsymbol{E}_0(\boldsymbol{x}) \in \mathrm{H}(\mathrm{curl}; \Omega)$, $H_0(\boldsymbol{x}) \in \mathrm{H}(\mathrm{rot}; \Omega)$, and where $\varepsilon, \mu \in \mathrm{L}^\infty(\Omega)$ are the dielectric permittivity and magnetic permeability, assumed to be scalar valued and time-invariant for simplicity of exposition. The vector field $\boldsymbol{J}(t, \boldsymbol{x})$ (assumed to be 0 in most of our numerical experiments, and for the sake of simplicity we assume $\boldsymbol{J} \in \mathrm{C}([0, T]; \mathrm{L}^2(\Omega))$ is the electric current density (a suitable a priori known source of the sytem) and $T > 0$ is the final simulation time. This is the system on which some of the authors also focused in [6] and provides also the most challenging test case for the new approach, since mass lumping for high order versions of edge elements is not as straightforward to achieve as for the scalar valued pressure in the acoustic case.

We point out that Eq. (9)–Eq. (12) is obtained using the transverse magnetic ansatz for the actual vector valued magnetic field (necessarily defined in a three-dimensional domain) to be of the form $\boldsymbol{H} = H\hat{\boldsymbol{z}}$, where $\hat{\boldsymbol{z}}$ is the unit vector in the z-direction and $H \in H(\mathrm{rot}; \Omega)$. By Galerkin testing and integration by parts of (9)–(10) (and neglecting current sources for the sake of brevity) on

each quadrilateral $K \in \mathcal{K}_h$, boundary integrals appear on the segments bounding K. We obtain the semi-discrete weak formulation to find $\boldsymbol{E}_h \in \tilde{X}_P^{\mathrm{curl}}(\tilde{\mathcal{T}}_h)$ and $H_h \in X_P^{\mathrm{rot}}(\mathcal{T}_h) := X_P^{\mathrm{grad}}(\mathcal{T}_h)$[1] such that:

$$\sum_{\tilde{T}\in\tilde{\mathcal{T}}_h}\sum_{K\subset\tilde{T}}\left\langle \varepsilon\frac{\partial \boldsymbol{E}_h}{\partial t},\boldsymbol{e}\right\rangle_K^P = \sum_{\tilde{T}\in\tilde{\mathcal{T}}_h}\left(\sum_{K\subset\tilde{T}}\int_K H_h\hat{\boldsymbol{z}}\cdot\operatorname{curl}\boldsymbol{e} + \sum_{F\in\partial\tilde{T}}\int_F \boldsymbol{e}\cdot H_h\hat{\boldsymbol{z}}\times\hat{\boldsymbol{n}}_K\right), \tag{13}$$

$$\sum_{K\in\mathcal{T}_h}\sum_{K\subset T}\left\langle \mu\frac{\partial H_h}{\partial t},h\right\rangle_K^P = \sum_{K\in\mathcal{T}_h}\left(\sum_{K\subset T}-\int_K \boldsymbol{E}_h\cdot\operatorname{rot} h + \sum_{F\in\partial T}\int_F \boldsymbol{E}_h\cdot h\hat{\boldsymbol{z}}\times\hat{\boldsymbol{n}}_K\right), \tag{14}$$

holding for all $\boldsymbol{e}\in\tilde{X}_P^{\mathrm{curl}}(\tilde{\mathcal{T}}_h)$, and $h\in X_P^{\mathrm{rot}}(\mathcal{T}_h)$, where $\hat{\boldsymbol{n}}_K$ denotes the outer normal on each element boundary. The above system implies weak imposition of the $\boldsymbol{E}_h\times\hat{\boldsymbol{n}}_\Omega = 0$ boundary conditions. We also require $\boldsymbol{E}_h|_{t=0}$ and $H_h|_{t=0}$ to fulfill the initial conditions through an L^2-projection at the initial time.

We close the subsection with a final important statement regarding the Maxwell system, which clarifies that the most succint way of writing its weak formulation, chosen in the manuscript, is not necessarily the most efficient one for the practical implementation.

Remark 3.1. For the implementation of the presented method one may apply integration by parts to Eq. (13). The reader may easily verify that in this case all the edge contributions which are not part of $\partial\tilde{T}$ for any $\tilde{T}\in\tilde{\mathcal{T}}$ cancel out. Thus, one is only left with integral contributions on either a triangle T, or its boundary ∂T, i.e., on the original triangulation assumed available from a FEM perspective. An implementation can therefore exploit existing finite element codes (as we did within Netgen/NGSolve, [10,11]), without explicitly having to generate the dual mesh.

3.2. Acoustic wave equations

In this section, we briefly sketch how the same method can be applied to the simulation of acoustic waves, without any practical differences in computational efficiency. Analogously to Section 3.1 we start from a strong formulation in the velocity-pressure first-order system form, i.e., the initial boundary value problem of finding $\boldsymbol{V}(t,\boldsymbol{x})\in\mathrm{C}^1([0,T];\mathrm{H}(\mathrm{div};\Omega))$ and $Q(t,\boldsymbol{x})\in\mathrm{C}^1([0,T];\mathrm{H}(\mathrm{grad};\Omega))$ such that:

$$\frac{\partial Q}{\partial t} = \rho_0 c^2\operatorname{div}\boldsymbol{V}, \qquad \text{in } \Omega\times(0,T), \tag{15}$$

$$\rho_0\frac{\partial \boldsymbol{V}}{\partial t} = \operatorname{grad} Q + \boldsymbol{f}, \qquad \text{in } \Omega\times(0,T), \tag{16}$$

$$\boldsymbol{V}\cdot\hat{\boldsymbol{n}}_\Omega = 0, \qquad \text{on } \partial\Omega\times(0,T), \tag{17}$$

$$\boldsymbol{V}(0,\boldsymbol{x}) = \boldsymbol{V}_0(\boldsymbol{x}), \quad Q(0,\boldsymbol{x}) = Q_0(\boldsymbol{x}), \qquad \text{in } \Omega, \tag{18}$$

with $\boldsymbol{V}\cdot\hat{\boldsymbol{n}}_\Omega = 0$, where Q is the acoustic pressure, $\boldsymbol{V}$ is the particle velocity, ρ_0 is the reference density, c is the speed of sound, both assumed to be in $\mathrm{L}^\infty(\Omega)$ and $\boldsymbol{f}(t,\boldsymbol{x})\in\mathrm{C}([0,T];\mathrm{L}^2(\Omega))$ is a suitable given forcing. We again have initial conditions $\boldsymbol{V}_0(\boldsymbol{x})\in\mathrm{H}(\mathrm{div};\Omega)$, $Q_0(\boldsymbol{x})\in\mathrm{H}(\mathrm{grad};\Omega)$. The semi-discrete weak formulation of Eq. (15)–Eq. (16) (again neglecting source terms) then seeks $Q_h\in X_P^{\mathrm{grad}}(\mathcal{T}_h)$ and $\boldsymbol{V}_h\in\tilde{X}_P^{\mathrm{div}}(\tilde{\mathcal{T}}_h)$ such that for all test functions $q\in X_P^{\mathrm{grad}}(\mathcal{T}_h)$ and $\boldsymbol{v}\in\tilde{X}_P^{\mathrm{div}}(\tilde{\mathcal{T}}_h)$:

$$\sum_{K\in\mathcal{T}_h}\sum_{K\subset T}\left\langle \frac{1}{\rho_0 c^2}\frac{\partial Q_h}{\partial t},q\right\rangle_K^P = \sum_{K\in\mathcal{T}_h}\left(\sum_{K\subset T}-\int_K \boldsymbol{V}_h\cdot\operatorname{grad} q + \sum_{F\in\partial T}\int_F q\,(\boldsymbol{V}_h\cdot\hat{\boldsymbol{n}}_K)\right),$$

$$\sum_{\tilde{T}\in\tilde{\mathcal{T}}_h}\sum_{K\subset\tilde{T}}\left\langle \rho_0\frac{\partial \boldsymbol{V}_h}{\partial t},\boldsymbol{v}\right\rangle_K^P = \sum_{\tilde{T}\in\tilde{\mathcal{T}}_h}\left(\sum_{K\subset\tilde{T}}-\int_K Q_h\operatorname{div}\boldsymbol{v} + \sum_{F\in\partial\tilde{T}}\int_F Q_h\,(\boldsymbol{v}\cdot\hat{\boldsymbol{n}}_K)\right),$$

holding for all $\boldsymbol{v}\in\tilde{X}_P^{\mathrm{div}}(\tilde{\mathcal{T}}_h)$, and $q\in X_P^{\mathrm{grad}}(\mathcal{T}_h)$, where $\hat{\boldsymbol{n}}_K$ denotes again the outer normal on each boundary of K. The above system implies weak imposition of the $\boldsymbol{V}_h\cdot\hat{\boldsymbol{n}}_\Omega = 0$ boundary conditions. We again also require $\boldsymbol{V}_h|_{t=0}$ and $Q_h|_{t=0}$ to fulfill the initial conditions through an L^2-projection at the initial time. Finally we stress that Remark 3.1 (with appropriate modifications) also hold for the acoustic case.

3.3. Related methods

Before putting the new mass lumped approach to the numerical test we dedicate a subsection to address the relationship, similarities and differences between the presented method and related approaches available in the literature. The proposed approach is,

[1] Even if redundant from functional analytic point of view in two dimensions, we still use the $X_P^{\mathrm{rot}}(\mathcal{T}_h)$ notation to recall that the differential operator involved is algebraically different.

as was the case for [6], based on the seminal work on low order barycentric dual grid methods in [5,12–14]. The barycentric dual is not the only choice that provides a possible extension to high order. In fact Chung and co-authors have championed staggered DG methods in several works on structured [15] and unstructured [16–18] grids, to obtain a penalty free approach which presents block-diagonal mass matrices. Nevertheless, in the very relevant unstructured case their underlying micro-cells, on which one exploits the same integration by parts formula are still triangles, since the Worsey–Farin split mesh is used. This can be a drawback in two ways: firstly, since each triangle corner is bisected, the shape-regularity constants degrade with respect to the original triangular mesh worsening the system's conditioning. In our case the shape-regularity constants of the new mesh are the same as the ones given by the initial FE mesh and less stringent than the ones of the Worsey–Farin split [19]. Secondly, improving the orthogonality of basis functions through mass lumping techniques amounts to finding an integration rule which allows an $\mathrm{H}(\mathrm{curl}, T)$-conforming (or $\mathrm{H}(\mathrm{div}, T)$-conforming for mixed formulation of the acoustic case) nodal basis on a Worsey–Farin split of a triangle to be constructed, which is ultimately just as hard as finding such a construction for a fully $\mathrm{H}(\mathrm{curl}, \Omega)$-conforming discrete space on the whole triangulation. Even though progress has been made recently in this regard with mass lumping schemes for acoustic and electromagnetic wave equations of higher order (see [20–22]), a general recipe for arbitrary polynomial degrees remained an open question. Our mass-lumping technique is formulated on a quadrilateral mesh and it therefore bypasses the issue completely by relying on tensor-product integration rules.

3.4. Time discretization

We turn our focus back to the Maxwell equations as an example for the time discretization, since the wave equation is treated in a completely analogous way. We remark that in both cases we achieve semidiscrete energy conservation properties, which can be shown trivially by the same integration by parts techniques used in [6]. Focusing then on the time discretization of Eq. (13), Eq. (14), the common leap frog scheme is used as a convenient choice to test the new mass lumping approach, since it is a very easy to implement symplectic integrator and it is second order accurate in time. If we denote with $\mathbf{h} \in \mathbb{R}^{\dim(X_P^{\mathrm{rot}}(\mathcal{T}_h))}$ and $\mathbf{e} \in \mathbb{R}^{\dim(\tilde{X}_P^{\mathrm{curl}}(\tilde{\mathcal{T}}_h))}$ the vectors of degrees of freedom for the magnetic and electric field respectively, appropriately ordered to evidence the block diagonal structures of the mass matrices, the scheme is given by the following update rules:

$$\mathbf{h}^{1/2} = \mathbf{h}^0 - \frac{\Delta t}{2}\mathbf{M}_\mu^{-1}\mathbf{C}\mathbf{e}^0,$$
$$\mathbf{e}^1 = \mathbf{e}^0 + \Delta t\,\mathbf{M}_\varepsilon^{-1}\mathbf{C}^\top\mathbf{h}^{1/2},$$

for the first update of the magnetic field and

$$\mathbf{h}^{n+1/2} = \mathbf{h}^{n-1/2} - \Delta t\,\mathbf{M}_\mu^{-1}\mathbf{C}\mathbf{e}^n,$$
$$\mathbf{e}^{n+1} = \mathbf{e}^n + \Delta t\,\mathbf{M}_\varepsilon^{-1}\mathbf{C}^\top\mathbf{h}^{n+1/2},$$

for all $n \geq 1$, in which $\mathbf{e}^n$ is the approximation computed at time instant $n\Delta t$ and $\mathbf{h}^{n+1/2}$ is computed at time instant $(n+1/2)\Delta t$, for $n = 0, \ldots, N$. The final time T is divided into N time steps of size $\Delta t = T/N$. Sparse matrix $\mathbf{C}$ is the matrix representation of the discrete curl operator, which is the r.h.s. of Eq. (14), while $\mathbf{M}_\mu$ and $\mathbf{M}_\varepsilon$ are the mass matrices for the magnetic and electric field respectively.

What we want to stress about the fully discrete formulation is that the l.h.s. gives rise to block diagonal system matrices $\mathbf{M}_\mu$ and $\mathbf{M}_\varepsilon$. They thus have block diagonalinverses where the block size does not increase with increasing polynomial degree, differently from what was achieved in previous work were scaled monomials were used as a basis.

In order to guarantee stability, the time step Δt is computed in such a way that

$$\Delta t < t_0 := 2/\sqrt{\lambda_M}, \tag{19}$$

where λ_M is the maximum of the eigenvalues λ of the eigenvalue problem

$$\mathbf{C}\mathbf{M}_\varepsilon^{-1}\mathbf{C}^\top\mathbf{h} = \lambda\mathbf{M}_\mu\mathbf{h}, \tag{20}$$

for the eigenvectors $\mathbf{h}$. The dependence of this so called Courant-Friedrichs-Lewy (CFL) condition on the discretization parameters is studied numerically in Section 4.2.

4. Numerical experiments

We perform several numerical experiments to underline the applicability, efficiency and convergence of our method. To this end we use an implementation of our method in the high-order finite element library Netgen/NGSolve [10,11] along the lines of Remark 3.1.

In particular, in Section 4.1 we show that we obtain spectral convergence of the underlying eigenvalue problem with polynomial convergence rates. The experiments in Section 4.2 study the dependence of the CFL condition on the discretization parameters, while Section 4.3 highlight the time-domain convergence. In Section 4.4 and Section 4.5 we study the computational efficiency and robustness of the mass lumping approach. Finally we present in Section 4.7 a more practical example where we also apply perfectly matched layers (PML) to simulate an open domain. The necessity of using PML to truncate the unbounded domain obviously

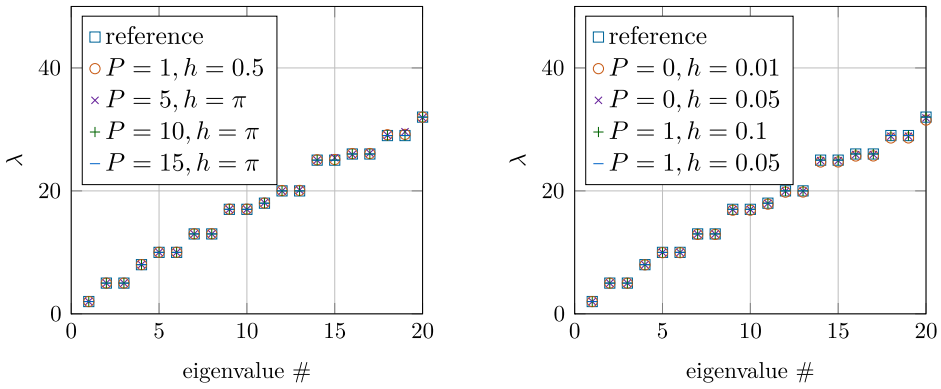

(a) coarse mesh, high order

(b) fine mesh, low order

Fig. 7. Spectra of the discrete Dirichlet Laplacian on the square $[0, \pi]^2$ with polynomial degree P and mesh size h.

introduces additional constraint of the CFL condition. We estimate the CFL condition numerically by power iteration in general for each simulation and use a smaller step that fulfills it. We do not discuss the influence of the PML on the method at length here since we make use of standard complex coordinate stretching techniques [23] and their advantages and drawbacks are not specific to the present method but are a shared theme for all methods using PMLs.

4.1. Eigenvalue problem

Since our main concern is the spatial discretization we perform experiments for the scalar discrete eigenvalue problem (EVP) (20) with $\mu = \varepsilon \equiv 1$.

This EVP is a discretization of the problem to find $\lambda \in \mathbf{R}$ and nontrivial $H \in H^1(\Omega)$ such that

$$-\Delta H = \lambda H, \qquad \text{on } \Omega, \tag{21}$$

$$H = 0, \qquad \text{on } \partial\Omega. \tag{22}$$

For our experiments we choose the square $\Omega = (0, \pi)^2$ where eigenpairs are given by

$$H_{n,k} = \sin(nx)\sin(ky), \qquad \lambda_{n,k} = n^2 + k^2, \qquad n, k \in \mathbf{N}^+. \tag{23}$$

Equivalenty we could derive the corresponding system for the acoustic case with $\rho_0 = c \equiv 1$ resulting in the problem to find $Q \in H^1(\Omega)$ such that

$$-\Delta Q = \lambda Q, \qquad \text{on } \Omega,$$

$$Q = 0, \qquad \text{on } \partial\Omega,$$

with the same eigenpair solutions and discrete matrix eigenvalue problem. Thus the numerical experiments for the EVP corresponding to the acoustic initial boundary value problem exhibit the same behavior as the ones corresponding to the electromagnetic one studied in the following subsections. We will therefore report only one set of results for the sake of brevity.

Fig. 7 shows the discrete spectra of the different discretizations of the eigenvalue problem Eqs. (21) and (22). We observe no spurious eigenvalues for large polynomials degrees or finer mesh sizes respectively, i.e., all discrete eigenvalues converge towards their continuous counterparts. Fig. 8 shows the convergence of selected discrete eigenvalues to their continuous counterparts. Note that while the experiments for degrees $P > 0$ suggest a convergence rate of order h^{2P} for the lowest order method we observe super convergence of the same order as for the method of order 1 (i.e., a rate of h^2, which was already observed in [6]). However the constant for the first order method improves significantly. Note that due to the high order convergence, in order to generate meaningful results (without hitting machine precision after very few refinements) we had to pick higher frequency resonances for the fourth order method.

Fig. 9 shows the convergence of one of the eigenvalues from Fig. 8d with respect to the degrees of freedom for different polynomial degrees, suggesting that for smooth solutions a high order method is efficient. Also it confirms that, although we have quadratic convergence in h for the polynomial degrees $P = 0, 1$, the method with $P = 1$ yields better results for the same number of degrees of freedoms.

4.2. CFL condition

Before we turn to time domain experiments we study numerically how the stability condition Eq. (19) on the timestep Δt depends on the discretization parameters h and P. Fig. 10 shows the dependence of the maximal stable timestep t_0 from Eq. (19)

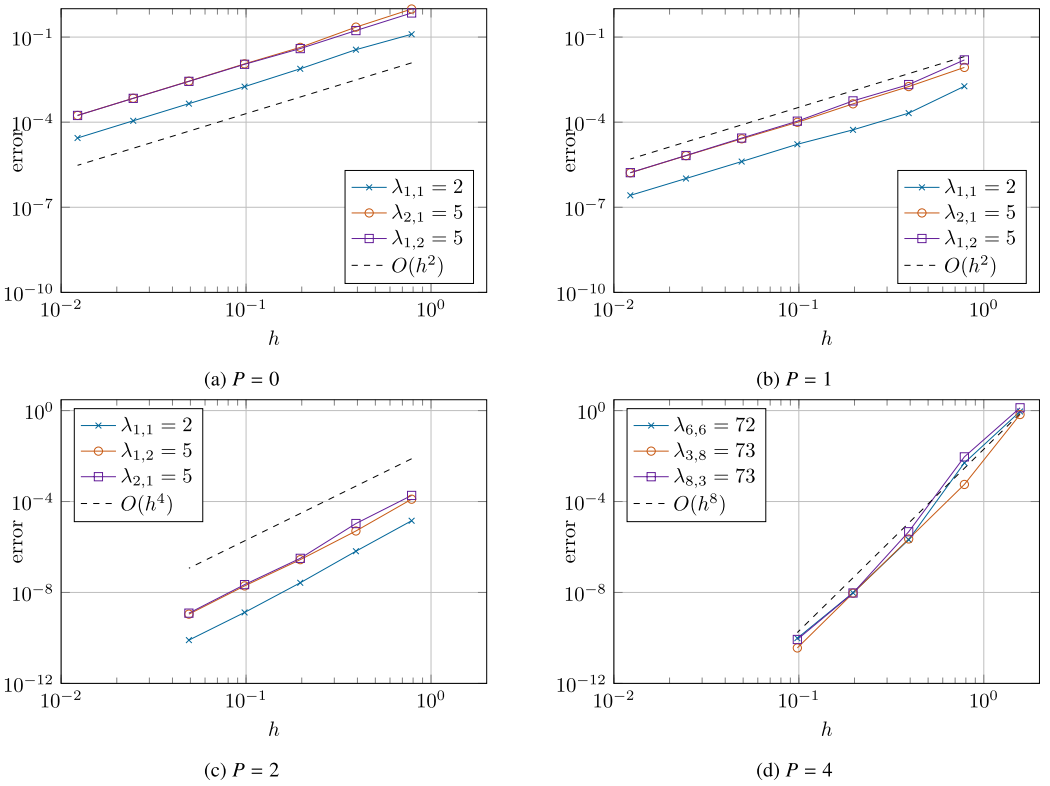

(a) $P = 0$ (b) $P = 1$

(c) $P = 2$ (d) $P = 4$

Fig. 8. Convergence of the absolute errors of discrete eigenvalues for polynomial degrees P and mesh sizes h.

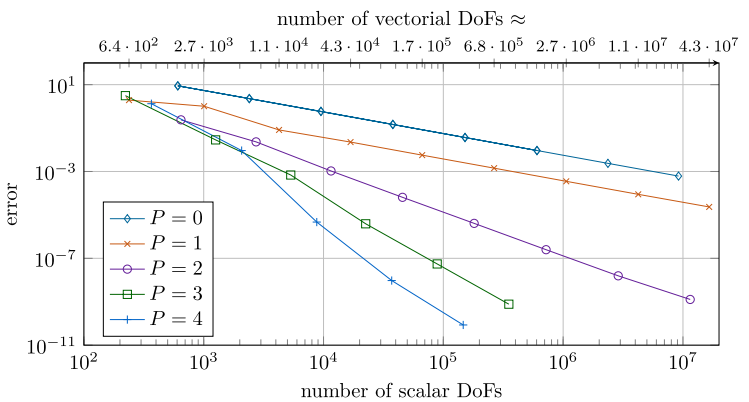

Fig. 9. Convergence with respect to the primal number of DoFs, for the eigenvalue $\lambda_{8,3} = 73$.

for $\Omega = (0,1)^2$ with homogeneous boundary conditions for H on the discretization parameters P and h. We clearly observe that $t_0 = O(h(P+1)^{-2})$ which is similar to the CFL condition for DG methods (cf., [3, Chapter 4.7]).

4.3. Time domain convergence

Fig. 11 shows the convergence of the time domain solution on $\Omega = (0,\pi)^2$ for a problem with initial conditions

$$H_0(x,y) = \sin(2x)\sin(y), \qquad \mathbf{E}_0(x,y) = 0,$$

at end time $T = 1$ and a leap frog timestepping with time-step $\tau = 10^{-5}$, which fulfills the CFL condition for all the used discretizations. We use relative errors measured in the discrete (mass-lumped) inner products given by Eqs. (5) and (6). We observe h^P convergence for all the studied quantities, except for the scalar field H, which measured in the discrete L^2-norm converges with h^{P+1}.

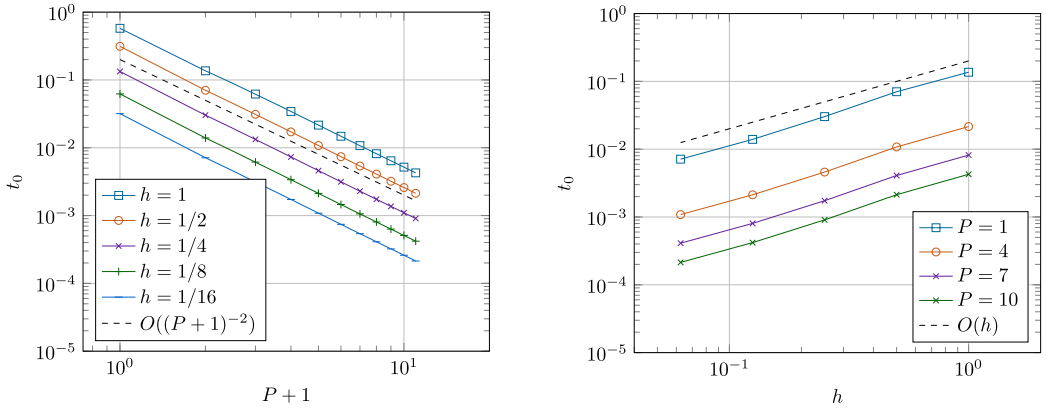

(a) fixed mesh-size h (b) fixed polynomial degree P

Fig. 10. The dependence of the maximal stable timestep t_0 on the discretization parameters.

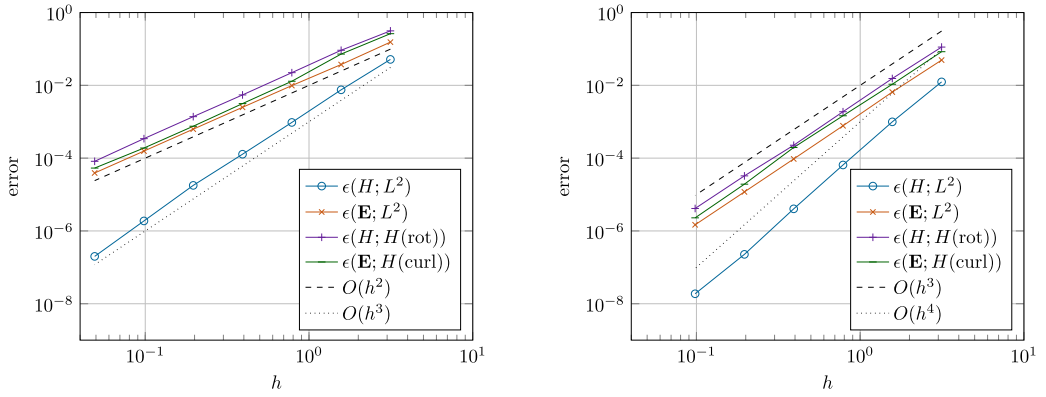

(a) $P = 2$ (b) $P = 3$

Fig. 11. Convergence of time domain solutions for polynomial orders $P = 2, 3$ with respect to different discrete norms.

4.4. Efficiency

To study the efficiency of using the mass lumped matrices we compare the number of non-zero entries of the mass matrices and the inverse matrices in the lumped and exact case respectively. To this end we choose a coarse mesh with six elements on the unit square and compare the number of non-zero entries in Fig. 12 for varying polynomial degree. We compare the matrices obtained by using the lumped inner products (cf., Section 2.2) to the ones obtained by exactly evaluating the integrals of the L^2 inner products. Since the lumped mass matrices are (block) diagonal with block sizes independent of the polynomial degree, we observe that the number of non-zero entries of the lumped mass matrices grows linearly with the number of degrees of freedom, even as the polynomial degree increases. The exact mass matrices are also block-diagonal, however, their block sizes grow with the polynomial degree (similar to the ones in [6]). For the exact mass matrix of the scalar variable we observe a growth of the non-zero entries per row of power $1/2$. For the remaining (inverse) mass matrices we observe a linear growth of non-zero entries per row with respect to the number of unknowns.

4.5. Robustness of computational efficiency

Due to the matrix-free nature of our method we expect to be able to do large scale computations without significant memory requirements.[2] Thus we expect the number of unknowns which can be computed per second to be independent of the number of finite elements (i.e., the mesh-size for a given problem). The efficiency of the inverse mass matrices is also independent of the polynomial degree while applying the discrete differential operators has a (mild) dependence on the polynomial degree. To test this we run a sequence of time dependent problems on the unit square with initial fields

[2] All computations were carried out on an off-the shelf desktop computer with 4 CPUs with 3.3 GHz and 16 GiB of memory.

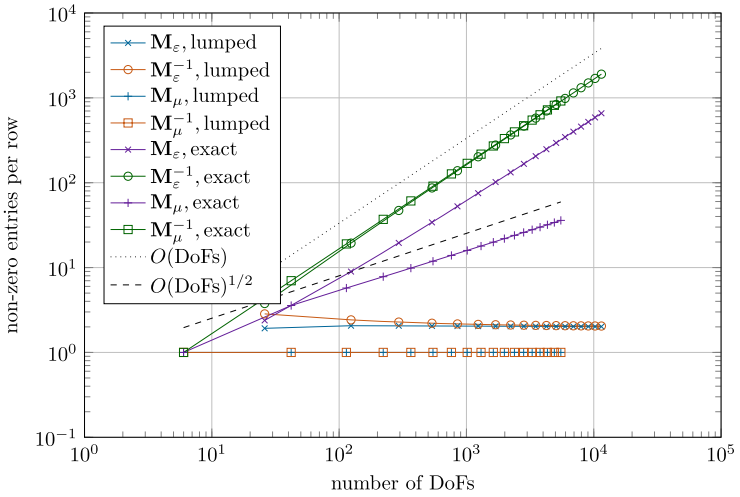

Fig. 12. Number of non-zero entries per row of the (inverse) mass matrices obtained by using exact and lumped integration for a mesh with $h = 0.5$ (six elements) and polynomial degrees P from 0 to 17.

Table 1
Computed DoFs/s for the initial value problem for different discretizations.

h	P	Δt	scal. DoFs	vect. DoFs	total DoFs	DoFs/s
$5 \cdot 10^{-2}$	4	$7 \cdot 10^{-4}$	$5.73 \cdot 10^{4}$	$1.27 \cdot 10^{5}$	$1.85 \cdot 10^{5}$	$1.71 \cdot 10^{8}$
$5 \cdot 10^{-2}$	5	$4 \cdot 10^{-4}$	$8.55 \cdot 10^{4}$	$1.87 \cdot 10^{5}$	$2.72 \cdot 10^{5}$	$1.4 \cdot 10^{8}$
$5 \cdot 10^{-2}$	6	$2 \cdot 10^{-4}$	$1.19 \cdot 10^{5}$	$2.57 \cdot 10^{5}$	$3.77 \cdot 10^{5}$	$1.14 \cdot 10^{8}$
$1 \cdot 10^{-2}$	2	$4 \cdot 10^{-4}$	$4.4 \cdot 10^{5}$	$1.04 \cdot 10^{6}$	$1.48 \cdot 10^{6}$	$1.32 \cdot 10^{8}$
$1 \cdot 10^{-2}$	3	$2 \cdot 10^{-4}$	$8.57 \cdot 10^{5}$	$1.95 \cdot 10^{6}$	$2.81 \cdot 10^{6}$	$1.26 \cdot 10^{8}$
$1 \cdot 10^{-2}$	4	$1.2 \cdot 10^{-4}$	$1.41 \cdot 10^{6}$	$3.13 \cdot 10^{6}$	$4.54 \cdot 10^{6}$	$1.19 \cdot 10^{8}$
$1 \cdot 10^{-2}$	5	$1 \cdot 10^{-4}$	$2.11 \cdot 10^{6}$	$4.59 \cdot 10^{6}$	$6.7 \cdot 10^{6}$	$1.06 \cdot 10^{8}$
$1 \cdot 10^{-2}$	6	$5 \cdot 10^{-5}$	$2.94 \cdot 10^{6}$	$6.33 \cdot 10^{6}$	$9.27 \cdot 10^{6}$	$9.38 \cdot 10^{7}$
$5 \cdot 10^{-3}$	1	$5 \cdot 10^{-4}$	$6.48 \cdot 10^{5}$	$1.67 \cdot 10^{6}$	$2.31 \cdot 10^{6}$	$1.17 \cdot 10^{8}$
$5 \cdot 10^{-3}$	2	$1.2 \cdot 10^{-4}$	$1.76 \cdot 10^{6}$	$4.17 \cdot 10^{6}$	$5.92 \cdot 10^{6}$	$1.14 \cdot 10^{8}$
$5 \cdot 10^{-3}$	3	$1 \cdot 10^{-4}$	$3.42 \cdot 10^{6}$	$7.77 \cdot 10^{6}$	$1.12 \cdot 10^{7}$	$1.09 \cdot 10^{8}$

$$H_0(x, y) = \exp\left(-50^2\left((x-0.5)^2 + (y-0.5)^2\right)\right), \qquad \mathbf{E}_0(x, y) = 0,$$

for different mesh-sizes and polynomial degrees. Snapshots of the resulting solution for $h = 0.01$, $P = 4$ is shown in Fig. 13. The step-sizes Δt are chosen experimentally such that the resulting discretization is stable. Table 1 gives the according numbers of DoFs per second, where for each entry the minimal time of computing four times 50 steps is given. While we observe a small decay of the number of DoFs/s for larger problems (probably due to the more costly application of the differential operators), the results confirm that for the given problem sizes the number of DoFs/s is roughly 10^8, mostly independent of the mesh-size h and polynomial P degree.

On a more qualitative note it can be observed in Fig. 13 that the width of the transported peak is preserved during the computation, i.e., we do not observe any numerical dispersion.

4.6. Long time experiments

Although a detailed dispersion analysis of the method is out of reach for the work at hand we present long-time experiments to – at least qualitatively – study the dispersive properties. Moreover this example provides a simple configuration for comparison of competing methods. To this end we use $\Omega := (0, 1)^2$ with initial values

$$H(0; x, y) = \exp(-400(y - 1/2)^2), \qquad \mathbf{E}(0; x, y) = \mathbf{0}$$

with homogeneous Neumann boundary conditions for the scalar field. Fig. 14 shows the mesh (mesh-size $h = 0.1$) and solution for $P = 2$ at $T = 1,150$ and a time-step $\tau = 5 \cdot 10^{-5}$. Note that since we do not aim for computational efficiency here, we chose the time-step finer than the CFL condition dictates to obtain a negligible time-discretization error at the end smaller than 10^{-4}. Fig. 15 shows comparisons between different polynomial orders for the same experiment at $x = 0$ and different end times. Apart from the linear method we observe dispersive effects for the different orders at different numbers of cycles.

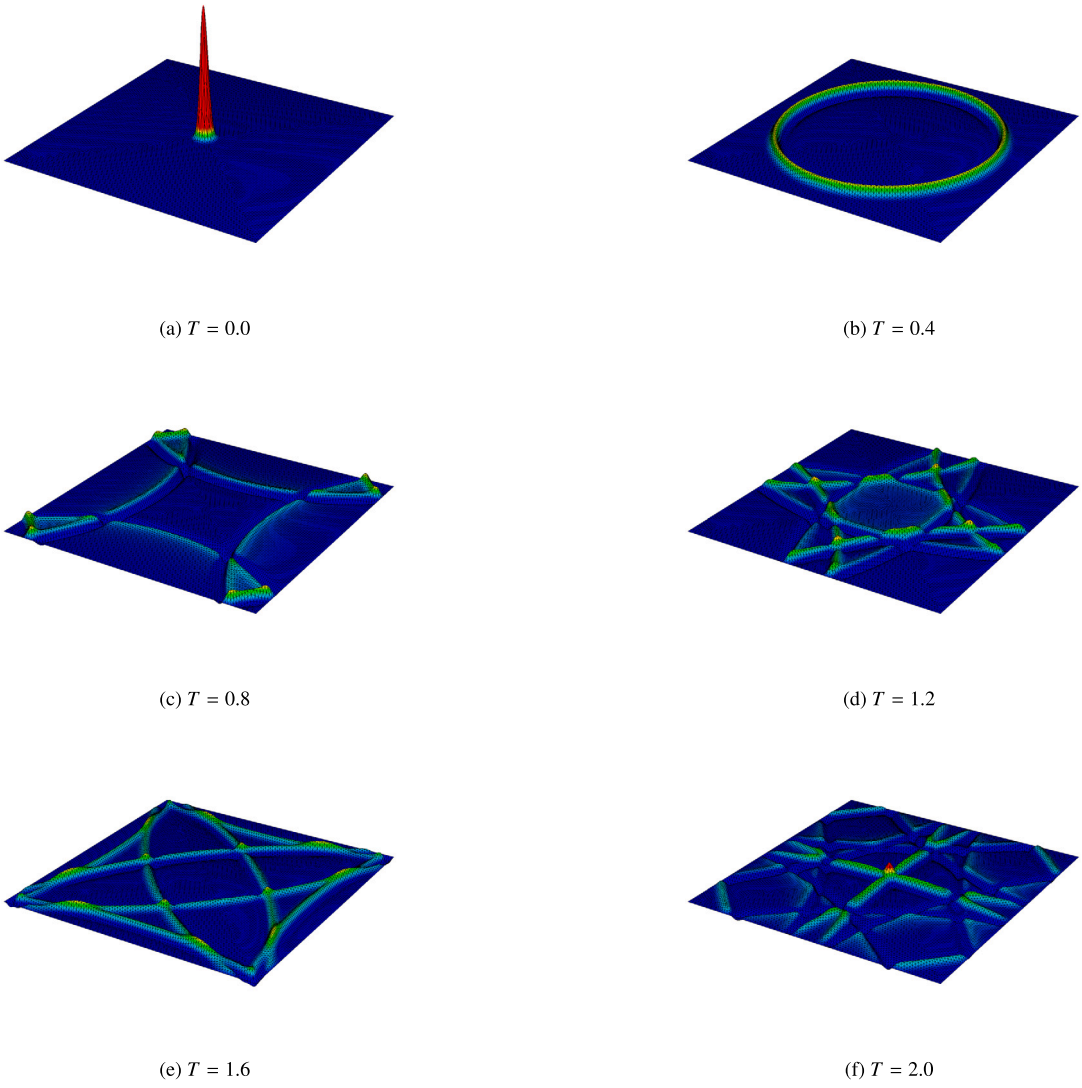

(a) $T = 0.0$ (b) $T = 0.4$

(c) $T = 0.8$ (d) $T = 1.2$

(e) $T = 1.6$ (f) $T = 2.0$

Fig. 13. Snapshots of the time domain solution for an inital Gauss peak for $t \in [0, 2]$.

(a) $T = 1$ (b) $T = 150$

Fig. 14. Propagation of a gaussian beam for polynomial order $P = 2$ after one and 150 cycles.

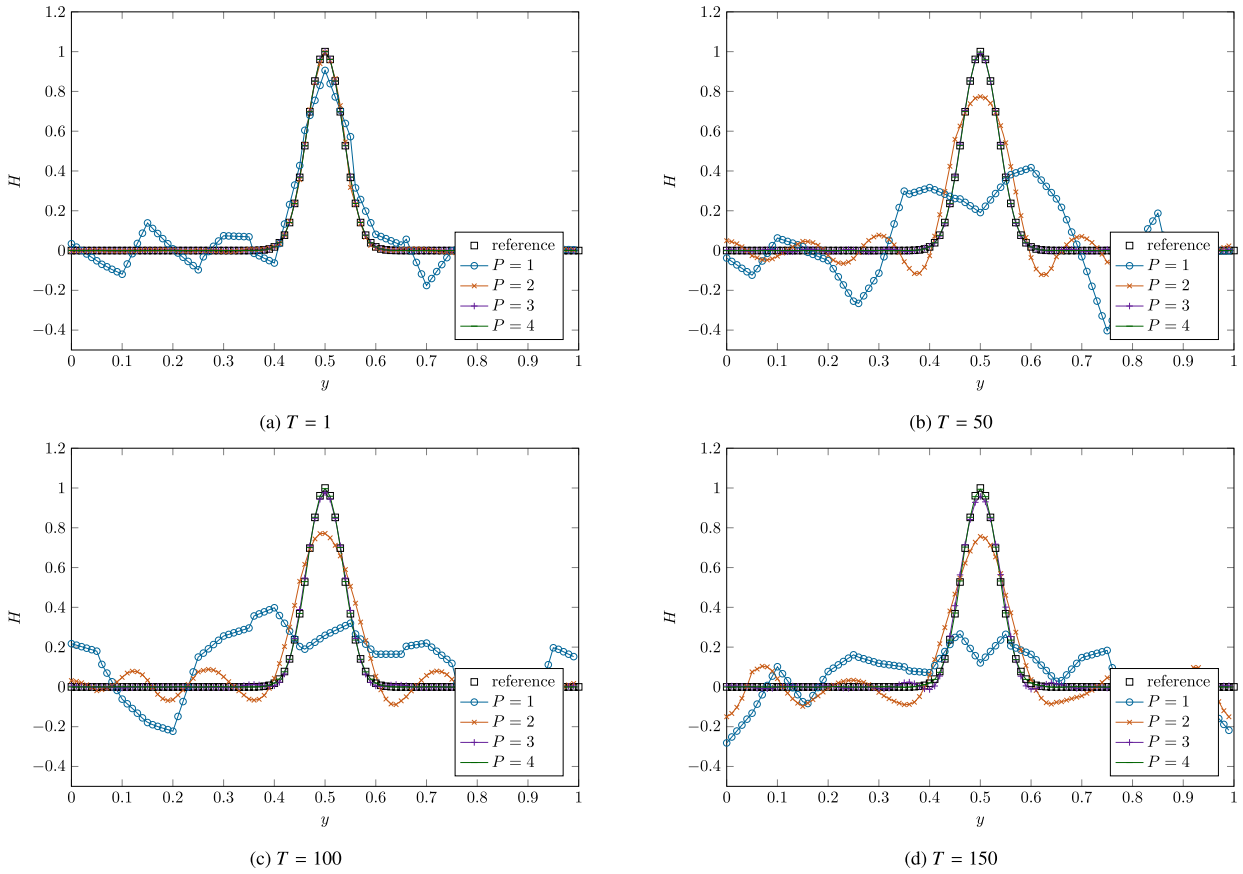

(a) $T = 1$ (b) $T = 50$

(c) $T = 100$ (d) $T = 150$

Fig. 15. Propagation of a gaussian beam for various polynomial orders and end times evaluated at $x = 0$ and values of y spaced 0.01 apart.

4.7. Ring resonator

To test our method in a more challenging setting we choose a model of a ring resonator, which is given by two parallel electrical wires with a looped wire in between (cf. Fig. 16a). We use the geometry parameters

$$a_x = 0.43, \qquad a_y = 0.405, \qquad b = 0.04, \qquad c = 0.035, \qquad p = 0.15, \qquad r_0 = 0.36, \qquad r_1 = 0.04,$$

and the material coefficients

$$\varepsilon_0 = 1, \qquad \varepsilon_1 = 9.$$

A wave is introduced at the left end of the top wire (cf. Fig. 16b)

$$f(t,y) = \begin{cases} \sin\left(\frac{\pi}{0.04}(y - a_y)\right) \frac{2e}{\sqrt{\pi}} \sin\left(\frac{10\pi}{\omega} t\right) \exp\left(-\frac{1}{1-(t-1)^2}\right), & t \le 2, \\ 0, & t > 2, \end{cases}$$

with $\omega = 1.542$. The wave resonates in the loop and induces an output at the left end of the bottom wire. The unbounded physical domain is modeled by the use of a perfectly matched layer (pml) (cf. [24,23]) with damping parameter $\sigma = 30$.

To obtain the results shown in Fig. 17 we use a mesh with $\approx 7.8 \cdot 10^3$ finite elements which results in spaces of dimension $\approx 7.1 \cdot 10^5$ for the scalar and $\approx 1.5 \cdot 10^6$ for the vectorial space when using a basis of order $P = 5$. Note that due to the auxiliary unknowns of the PML formulation the number of total unknowns is even higher. We choose a time-step size $\Delta t = 1.15 \cdot 10^{-4}$ which is experimentally confirmed to be stable (i.e., the CFL condition is fulfilled). Thus to compute up to $t = 12$, a number of $\approx 1.0 \cdot 10^5$ timesteps have to be computed. All computations were carried out on a desktop computer in less than a day of computation time, with one timestep taking $\approx 0.46s$. Due to the efficiency of the mass lumped basis the amount of used memory and time to set up the problem is negligible since no large (inverse) matrix has to be set up/stored.

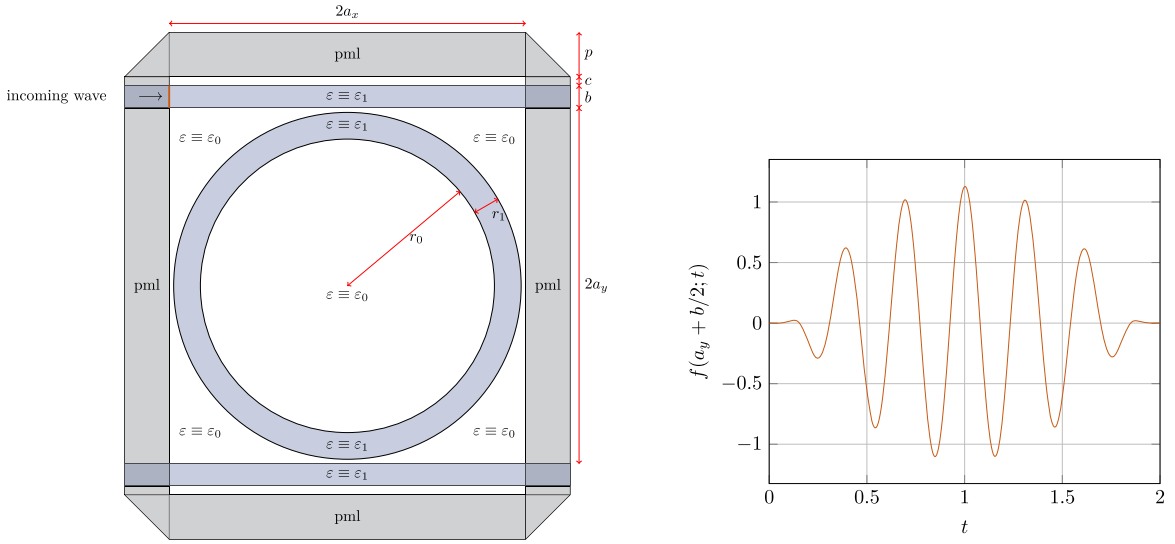

Fig. 16. Configuration of the ring resonator experiment.

5. Conclusion and outlook

In the work at hand we have presented a new approach to construct basis functions for an arbitrary order accurate (in the spacial discretization) cell method. In particular, this new basis resolves some stability issues from previous approaches and has the additional property that mass lumping is easily available for the respective mass matrices. Therefore our new approach results in well-conditioned (inverse) mass matrices with a very favorable sparsity pattern which is uniform in the polynomial degree of the basis. We introduced the resulting mass lumped formulation both, for the time domain Maxwell system and for the acoustic wave equation. We have applied our method in numerous numerical experiments to underline these claims and shown that the method scales very well for larger problems even on off-the-shelf desktop computers. Future work includes the extension of our method to higher dimensions for acoustic, as well as electromagnetic problems. We aim at optimizing the simulation of unbounded domains by using more sophisticated PML constructions such as the ones based on infinite elements of [25,26] and exploring alternative approximation techniques on quadrilateral elements such as spline approximations of curved boundaries, e.g., [27] or [28]. Finally, the theoretical numerical analysis of the method is being carried out and will be presented elsewhere.

CRediT authorship contribution statement

Markus Wess: Writing – review & editing, Writing – original draft, Visualization, Software, Methodology, Investigation, Conceptualization. **Bernard Kapidani:** Writing – review & editing, Writing – original draft, Visualization, Validation, Methodology, Investigation, Conceptualization. **Lorenzo Codecasa:** Writing – review & editing, Methodology, Investigation, Conceptualization. **Joachim Schöberl:** Writing – review & editing, Validation, Supervision, Software, Methodology, Investigation, Conceptualization.

Declaration of competing interest

The authors declare that they have no known competing financial interests or personal relationships that could have appeared to influence the work reported in this paper.

Data availability

Data will be made available on request.

Acknowledgements

Author Bernard Kapidani has been partially supported by the Swiss National Science Foundation via the project HOGAEMS n. 200021_188589.

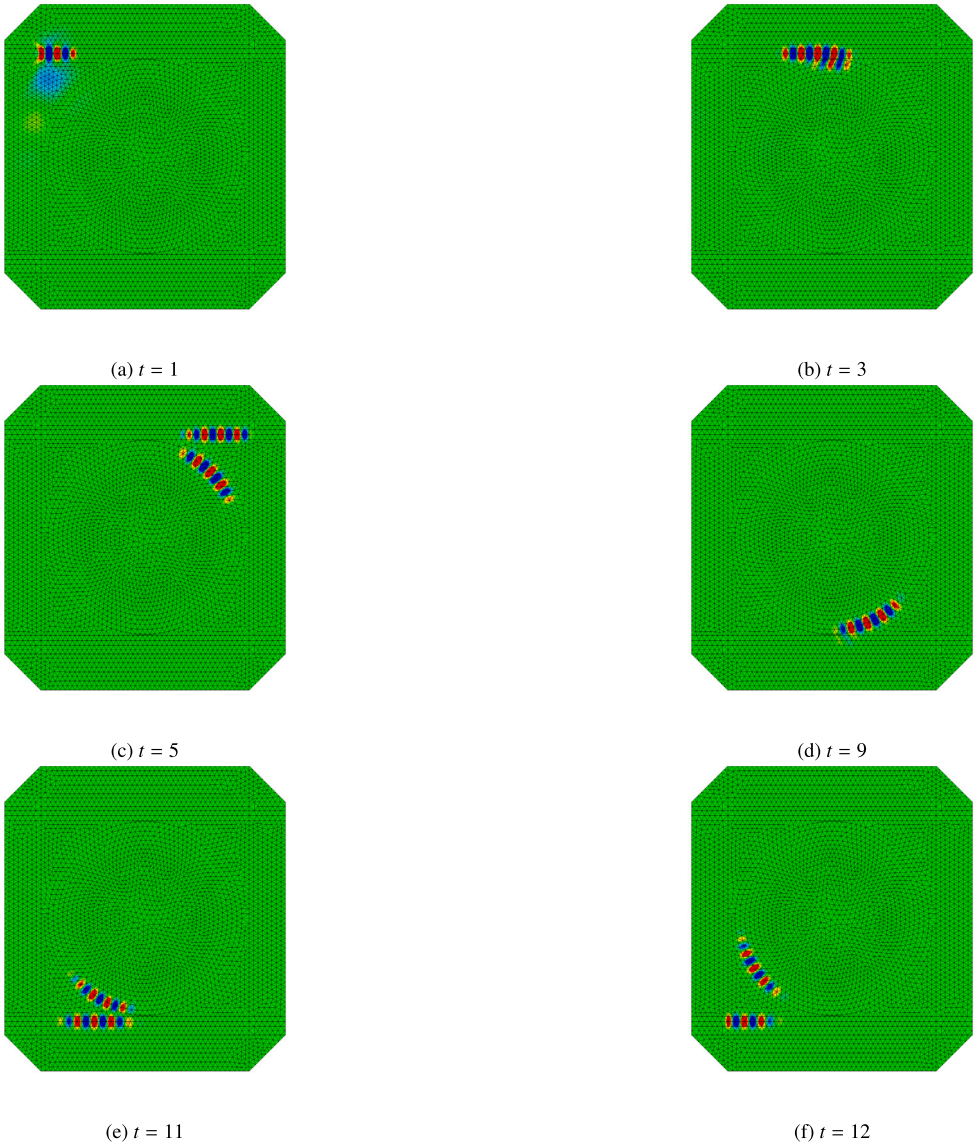

Fig. 17. Snapshots of the ring resonator experiments (cf., Fig. 16).

References

[1] J.D. Joannopoulos (Ed.), Photonic Crystals: Molding the Flow of Light, 2nd ed., Princeton University Press, Princeton, 2008.
[2] A. Taflove, A. Oskooi, S.G. Johnson (Eds.), Advances in FDTD Computational Electrodynamics: Photonics and Nanotechnology, Artech House, Boston, 2013.
[3] J. Hesthaven, T. Warburton, Nodal Discontinuous Galerkin Methods, Texts in Applied Mathematics, vol. 54, Springer, New York, New York, NY, 2008.
[4] T. Weiland, Time domain electromagnetic field computation with finite difference methods, Int. J. Numer. Model. Electr. Netw. Devices Fields 9 (1996) 295–319.
[5] L. Codecasa, M. Politi, Explicit, consistent, and conditionally stable extension of FD-TD to tetrahedral grids by FIT, IEEE Trans. Magn. 44 (2008) 1258–1261.
[6] B. Kapidani, L. Codecasa, J. Schöberl, An arbitrary-order Cell Method with block-diagonal mass-matrices for the time-dependent 2D Maxwell equations, J. Comput. Phys. 433 (2021) 110184.
[7] P.G. Ciarlet, The Finite Element Method for Elliptic Problems, Society for Industrial and Applied Mathematics, 2002, https://epubs.siam.org/doi/abs/10.1137/1.9780898719208, arXiv:https://epubs.siam.org/doi/pdf/10.1137/1.9780898719208.
[8] L. Demkowicz, P. Monk, L. Vardapetyan, W. Rachowicz, De Rham diagram for *hp* finite element spaces, Comput. Math. Appl. 39 (2000) 29–38.
[9] E. Süli, D. Mayers, An Introduction to Numerical Analysis, Cambridge University Press, 2003.
[10] J. Schöberl, Netgen - an advancing front 2d/3d-mesh generator based on abstract rules, Comput. Vis. Sci. 1 (1997) 41–52.
[11] J. Schöberl, C++11 Implementation of Finite Elements in NGSolve, Institute of Analysis and Scientific Computing, TU Wien, 2014, Preprint 30/2014.
[12] L. Codecasa, B. Kapidani, R. Specogna, F. Trevisan, Novel FDTD technique over tetrahedral grids for conductive media, IEEE Trans. Antennas Propag. 66 (2018) 5387–5396.
[13] M. Cicuttin, L. Codecasa, B. Kapidani, R. Specogna, F. Trevisan, GPU accelerated time-domain discrete geometric approach method for Maxwell's equations on tetrahedral grids, IEEE Trans. Magn. 54 (2018) 1–4.
[14] B. Kapidani, L. Codecasa, R. Specogna, The time-domain cell method is a coupling of two explicit discontinuous Galerkin schemes with continuous fluxes, IEEE Trans. Magn. 56 (2020) 1–4.

[15] E.T. Chung, P. Ciarlet, T. Yu, Convergence and superconvergence of staggered discontinuous Galerkin methods for the three-dimensional Maxwell's equations on Cartesian grids, J. Comput. Phys. 235 (2013) 14–31.
[16] E.T. Chung, B. Engquist, Optimal discontinuous Galerkin methods for the acoustic wave equation in higher dimensions, SIAM J. Numer. Anal. 47 (2009) 3820–3848.
[17] B. Cockburn, G.E. Karniadakis, C.W. Shu (Eds.), Discontinuous Galerkin Methods: Theory, Computation and Applications, Springer Science & Business Media, 2012.
[18] E. Chung, B. Cockburn, G. Fu, The staggered DG method is the limit of a hybridizable DG method, SIAM J. Numer. Anal. 52 (2014) 915–932.
[19] S. Gong, J. Guzmán, M. Neilan, A note on the shape regularity of Worsey–Farin splits, J. Sci. Comput. 95 (2023) 46.
[20] S. Geevers, W.A. Mulder, J.J.W. Van Der Vegt, New higher-order mass-lumped tetrahedral elements for wave propagation modelling, SIAM J. Sci. Comput. 40 (2018) A2830–A2857.
[21] H. Egger, B. Radu, A mass-lumped mixed finite element method for acoustic wave propagation, Numer. Math. 145 (2020) 239–269.
[22] H. Egger, B. Radu, A second-order finite element method with mass lumping for Maxwell's equations on tetrahedra, SIAM J. Numer. Anal. 59 (2021) 864–885.
[23] F.L. Teixeira, W.C. Chew, Complex space approach to perfectly matched layers: a review and some new developments, Int. J. Numer. Model. Electr. Netw. Devices Fields 13 (2000) 441–455.
[24] J.P. Berenger, A perfectly matched layer for the absorption of electromagnetic waves, J. Comput. Phys. 114 (1994) 185–200.
[25] A. Bermúdez, L. Hervella-Nieto, A. Prieto, R. Rodríguez, An optimal perfectly matched layer with unbounded absorbing function for time-harmonic acoustic scattering problems, J. Comput. Phys. 223 (2007) 469–488.
[26] L. Nannen, M. Wess, Complex-scaled infinite elements for resonance problems in heterogeneous open systems, Adv. Comput. Math. 48 (2022) 8.
[27] A. Ratnani, E. Sonnendrücker, An arbitrary high-order spline finite element solver for the time domain Maxwell equations, J. Sci. Comput. 51 (2012) 87–106.
[28] B. Kapidani, R. Vázquez, High order geometric methods with splines: fast solution with explicit time-stepping for Maxwell equations, J. Comput. Phys. 493 (2023) 112440.